

AD-A272 329

FATATION PAGE

Form Approved
OMB No. 0704-0188

per response, including the time for reviewing instructions, searching existing data sources, gathering and maintaining the data needed for the burden estimate or any other aspect of the collection of information, including suggestions for reducing the burden to Washington Headquarters Services, Directorate for Information Operations and Reports, 1215 Jefferson Davis Highway, Suite 1200, Arlington, VA 22202-4302 and to the Office of Management and Budget, Paperwork Reduction Project 0704-0188, Washington, DC 20503.

1. AGENCY USE ONLY (Leave blank)	2. REPORT DATE 3 NOVEMBER 1993	3. REPORT TYPE AND DATES COVERED JOURNAL ARTICLE
4. TITLE AND SUBTITLE POLARIMETRIC SYNTHETIC APERTURE RADAR IMAGING		5. FUNDING NUMBERS C — F19628-90-C-0002 PE — 62702E, 62204F
6. AUTHOR(S) L.M.NOVAK; C.M.NETISHEN		
7. PERFORMING ORGANIZATION NAME(S) AND ADDRESS(ES) Lincoln Laboratory, MIT P.O. Box 73 Lexington, MA 02173-9108		8. PERFORMING ORGANIZATION REPORT NUMBER JA-6854
9. SPONSORING/MONITORING AGENCY NAME(S) AND ADDRESS(ES) ADVANCED RESEARCH PROJECTS AGENCY 3701 N.FAIRFAX DRIVE ARLINGTON, VA 22203		10. SPONSORING/MONITORING AGENCY REPORT NUMBER ESC-TR- 93-288
11. SUPPLEMENTARY NOTES INTERNATIONAL JOURNAL OF IMAGING SYSTEMS AND TECHNOLOGY, VOL.4, 306-318 (1992)		
12a. DISTRIBUTION/AVAILABILITY STATEMENT Approved for public release; distribution is unlimited.		12b. DISTRIBUTION CODE
13. ABSTRACT (Maximum 200 words) MIT Lincoln Laboratory is investigating the detection and identification of stationary ground targets in high resolution, fully polarimetric, synthetic aperture radar (SAR) imagery. This article (1) provides a brief description of the Lincoln Laboratory SAR, (2) describes an optimum polarimetric processing technique used to construct minimum-speckle SAR intensity imagery, and (3) presents examples of polarimetrically processed imagery. © 1993 John Wiley & Sons, Inc.		
14. SUBJECT TERMS SYNTHETIC APERTURE RADAR; SPECKLE REDUCTION; RADAR IMAGING; POLARIMETRIC WHITENING FILTER		15. NUMBER OF PAGES 14
17. SECURITY CLASSIFICATION OF REPORT Unclassified		18. SECURITY CLASSIFICATION OF THIS PAGE Unclassified
19. SECURITY CLASSIFICATION OF ABSTRACT Unclassified		20. LIMITATION OF ABSTRACT

DISCLAIMER NOTICE



**THIS DOCUMENT IS BEST
QUALITY AVAILABLE. THE COPY
FURNISHED TO DTIC CONTAINED
A SIGNIFICANT NUMBER OF
COLOR PAGES WHICH DO NOT
REPRODUCE LEGIBLY ON BLACK
AND WHITE MICROFICHE.**

Polarimetric Synthetic Aperture Radar Imaging*

L.M. Novak and C.M. Netishen

MIT Lincoln Laboratory, P.O. Box 73, Lexington, Massachusetts 02173-9108

93-27269



*Original contains color
plates: All DTIC reproductions will be in black and white.

ABSTRACT

MIT Lincoln Laboratory is investigating the detection and identification of stationary ground targets in high resolution, fully polarimetric, synthetic aperture radar (SAR) imagery. This article (1) provides a brief description of the Lincoln Laboratory SAR, (2) describes an optimum polarimetric processing technique used to construct minimum-speckle SAR intensity imagery, and (3) presents examples of polarimetrically processed imagery. © 1993 John Wiley & Sons, Inc.

I. INTRODUCTION

The Lincoln Laboratory SAR is a fully polarimetric, 33-GHz synthetic aperture radar sensor [1]. The polarimetric capability of the radar is used to enhance the quality of the imagery taken from a small aircraft; the synthetic aperture permits data to be processed to a resolution of 1 ft × 1 ft at a slant range of 7 km. The sensor was developed to provide a high-quality database of clutter and target-in-clutter imagery, for use in evaluating the performance of stationary-target detection, discrimination, and identification algorithms.

An example of the quality of imagery gathered by the SAR is presented in Fig. 1. This synthetic aperture radar image of a golf course located near Stockbridge, NY, has undergone the optimum speckle-reduction processing described here. Figure 2 shows a close-up photograph of the golf course; note the pond, flag pole, putting green, and line of four trees which are visible in both Figs. 1 and 2. Because of its high resolution, the Lincoln Laboratory SAR can resolve individual trees and bushes, as well as the pond and the putting green shown in the image. Note the 1 ft × 1 ft resolution permits one to discern very small objects such as the flag pole located in the center of the putting green. This image was obtained under clear weather conditions. However, the quality and resolution of the SAR image would not be degraded in the presence of dense fog or thick cloud cover. Thus a SAR sensor has a significant advantage over optical sensors: the image quality is not dependent on weather conditions, and the sensor can be used either during the day or at night.

Figure 3 shows the Lincoln Laboratory SAR Sensor and lists some of the system parameters. The SAR Sensor is an airborne, instrumentation-quality radar carried on a Gulf-

stream G1 aircraft. The radar antenna is housed in a specially designed radome mounted beneath the aircraft. The radar transmitter, dual-channel receiver, and digital recording equipment are all carried by the airplane.

Since a principal objective of the Lincoln Laboratory studies is to evaluate the benefits of fully polarimetric radar data for stationary-target detection and identification, polarization purity is essential. To achieve polarization purity, a special corrugated horn antenna with a Fresnel lens was designed, providing very pure horizontally and vertically polarized transmit waves. The radome was designed to minimize cross coupling between the horizontal and vertical polarizations. The radar transmits horizontal and vertical polarizations on alternate pulses; dual receiver channels measure both returns simultaneously. Inertial velocity estimates compensate for aircraft motion between the horizontal and vertical transmit pulses.

An in-scene corner reflector calibration array comprised of several high-quality trihedrals—and dihedrals oriented at 0, 22.5, and 45°—is used for polarimetrically calibrating the imagery. The polarimetric calibration scheme is described in ref. 2. During each flight, data are gathered and digitized in real time with a 28-channel Ampex recorder. The data are then brought to the Lincoln Laboratory ground processing facility, where SAR image formation is performed. Special-purpose, high-speed digital processing hardware is used to construct the imagery and perform the polarimetric calibration.

A SAR is a radar that synthesizes a long aperture as an aircraft flies along its path. Thus a SAR can achieve cross-range resolutions that could otherwise be attained only with a long antenna. In SAR mode the Lincoln Laboratory radar has 1 ft × 1 ft resolution. Range resolution is achieved by using 600-MHz bandwidth pulses. To achieve 1 ft azimuth resolution, a synthetic aperture of approximately 150 m length is constructed by processing 1 s of data as the plane flies.

SAR processing can produce high-resolution images, but the process is subject to a considerable amount of speckle in the images because of the coherent nature of the imaging process. Noncoherent spatial averaging of high-resolution pixel intensities can be used to reduce image speckle. For example, we have significantly reduced image speckle by averaging 4 × 4 pixel clusters of single-polarimetric-channel intensity data into effective 1-m × 1-m resolution pixels. However, the speckle reduction was obtained at the cost of degraded image resolution. A new technique described here, the polarimetric whitening filter (PWF), uses a polarimetric

*This work was sponsored by the Defense Advanced Research Projects Agency under Air Force Contract #F19628-90-C-0002.

Received 1 July 1992; revised manuscript received 3 November 1992

International Journal of Imaging Systems and Technology, Vol. 4, 306-318 (1992)
 © 1993 John Wiley & Sons, Inc.

CCC 0899-9457/93/040306-13

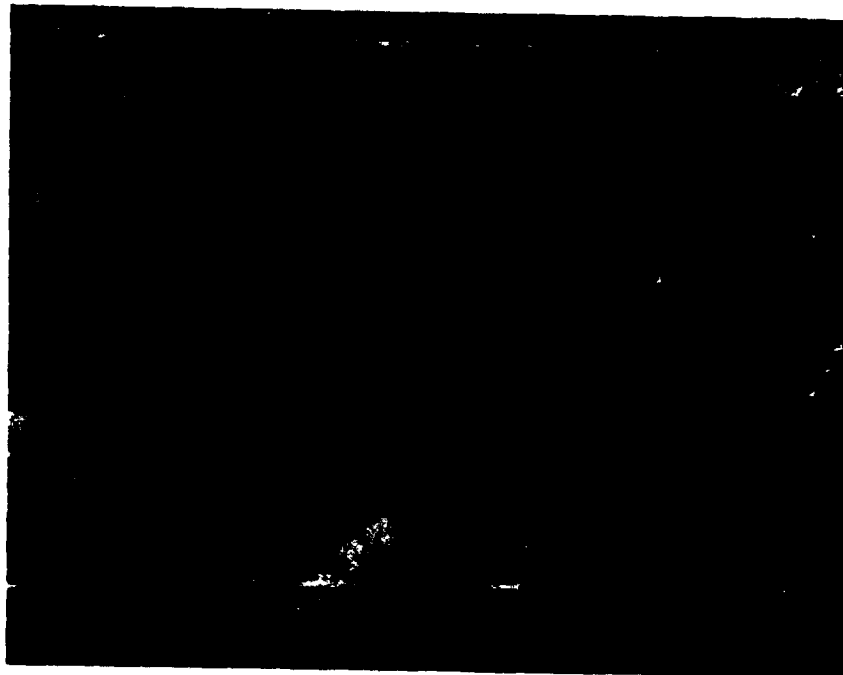


Figure 1. SAR image of a golf course in Stockbridge, NY (1 ft \times 1 ft resolution). The sensor was flown at an altitude of 2 Km with a look-down (depression) angle of 22.5°, giving a slant range of 7 Km. PWF processing was used to produce this minimum speckle image. The radar is located at the top of the image looking down, therefore, the radar shadows go toward the bottom of the page.

method of speckle reduction that preserves image resolution [3, 4]. This filter processes the complex (HH , HV , VV) data into full-resolution pixel intensities in a way that minimizes SAR image speckle. This method is based on a mathematical

model that characterizes fully polarimetric radar returns from clutter. By using this polarimetric clutter model, we can derive an algorithm that shows how fully polarimetric data can be combined into minimum-speckle imagery.



Figure 2. Optical photograph of one side of the golf course. This photograph was taken on November 1991. Some visible features in the photograph are the flag pole in the center of the putting green, the open area pond, and the four large trees adjacent to the pond.

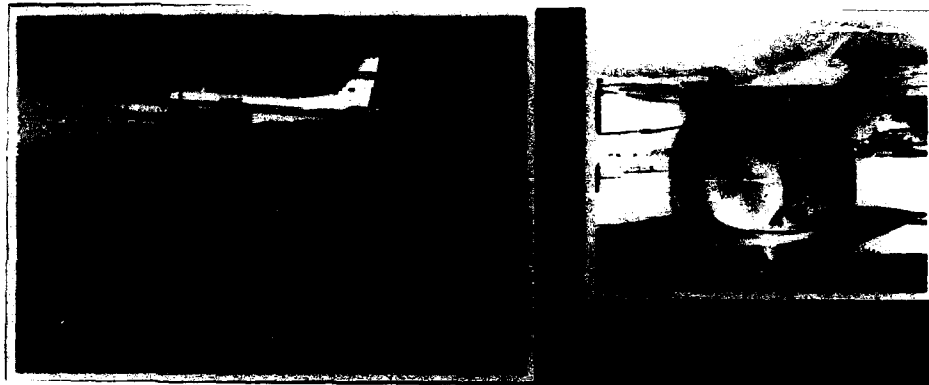


Figure 3. The advanced detection technology sensor (right). The sensor platform is a Gulfstream G1 aircraft shown in flight (left). The ADTS radome, located at the bottom of the aircraft, was built by the Loral Corporation. System features: SAR/RAR operation; coherent and fully polarimetric. System parameters: frequency, 33 GHz; resolution (SAR), 1 ft \times 1 ft; beamwidth, 2°; polarization isolation, 30 dB; sensitivity (SAR Mode), S/N 10 dB for (7 km Range), $\sigma = -30$ dB m².

II. POLARIMETRIC CLUTTER MODEL

We use a non-Gaussian "product" model to characterize the polarimetric return from ground clutter. Note that with a Gaussian model, each pixel of clutter in a spatially homogeneous region of an image has the same average polarimetric power. A number of authors have stated that it is more realistic to assume that ground clutter and sea clutter, for example, are spatially nonhomogeneous. A non-Gaussian model consistent with this more realistic assumption has been proposed [5-7], and, in fact, the Gaussian model is actually a special case of the non-Gaussian model.

We assume that the radar measurement vector \mathbf{Y} consists of three complex elements: HH , HV , and VV . Therefore,

$$\mathbf{Y} = \begin{pmatrix} HH \\ HV \\ VV \end{pmatrix} = \begin{pmatrix} HH_I + jHH_Q \\ HV_I + jHV_Q \\ VV_I + jVV_Q \end{pmatrix} \quad (1)$$

where HH_I and HH_Q , for example, are the in-phase and quadrature components of the complex HH measurement. \mathbf{Y} is assumed to be the product of a complex Gaussian vector \mathbf{X} (representing the speckle) and a spatially varying texture variable \sqrt{g} . That is,

$$\mathbf{Y} = \sqrt{g}\mathbf{X}. \quad (2)$$

The vector \mathbf{X} is assumed to be circular complex Gaussian with a joint probability density function (PDF) of the form:

$$f(\mathbf{X}) = \frac{1}{\pi^3 |\Sigma|} \exp(-\mathbf{X}' \Sigma^{-1} \mathbf{X}) \quad (3)$$

where $\Sigma = (\mathbf{X}\mathbf{X}')$ is the polarization covariance matrix. The vector \mathbf{X} is zero mean ($E(\mathbf{X}) = 0$). The covariance matrix that we use for clutter data takes the following form (in a linear-polarization basis):

$$\Sigma = \sigma_{mm} \cdot \begin{pmatrix} 1 & 0 & \rho\sqrt{\gamma} \\ 0 & \epsilon & 0 \\ \rho^*\sqrt{\gamma} & 0 & \gamma \end{pmatrix} \quad (4)$$

where

$$\sigma_{mm} = E(|HH|^2), \epsilon = \frac{E(|HH|^2)}{E(|HV|^2)}, \gamma = \frac{E(|VV|^2)}{E(|HH|^2)},$$

$$\text{and } \rho = \frac{E(HH \cdot VV^*)}{[E(|HH|^2) \cdot E(|VV|^2)]^{1/2}}. \quad (5)$$

The assumption that HV is uncorrelated with HH and VV is not always true (especially for man-made targets or for a polarimetric SAR with cross-talk between channels); however, we have found this assumption is valid for natural ground clutter.

We model the product multiplier g as a gamma-distributed random variable. This assumption is not universal; the log-normal and Weibull models are also widely used. But if we assume that the gamma distribution is reasonable, the PDF of the product multiplier g is specified by

$$f_{\tilde{g}}(g) = \frac{1}{\tilde{g}} \left(\frac{g}{\tilde{g}} \right)^{\nu-1} \frac{1}{\Gamma(\nu)} \exp\left(-\frac{g}{\tilde{g}}\right) \quad (6)$$

where the parameters \tilde{g} and ν are related to the mean and variance of the random variable g :

$$E(g) = \tilde{g}\nu$$

$$E(g^2) = \tilde{g}^2\nu(\nu+1). \quad (7)$$

With the assumption that g is gamma distributed, the PDF of the resulting vector $\mathbf{Y} = \sqrt{g}\mathbf{X}$ is the modified Bessel function, or generalized K -distribution [5].

$$f(\mathbf{Y}) = \frac{2}{\pi^3 \tilde{g}^3 \Gamma(\nu) |\Sigma|} \cdot \frac{K_{3-\nu} \left(2\sqrt{\frac{\mathbf{Y}' \Sigma^{-1} \mathbf{Y}}{\tilde{g}}} \right)}{(\tilde{g} \mathbf{Y}' \Sigma^{-1} \mathbf{Y})^{(3-\nu)/2}}. \quad (8)$$

If we set $\tilde{g} = (1/\nu)$ so that the mean of the texture variable is unity, then in the limit as $\nu \rightarrow \infty$, this model reduces to the Gaussian model.

III. MINIMUM-SPECKLE SAR IMAGE PROCESSING

In this section we consider how to process the three complex measurements— HH , HV , and VV (i.e., the vector \mathbf{Y})—into pixel intensity in a way that minimizes speckle. The clutter product model is used to derive the optimal method of polarimetric speckle reduction, which can be interpreted as a PWF. Then the amount of speckle reduction that can be achieved by using the PWF is determined theoretically.

The measure of speckle we use is the ratio of the standard deviation of the image pixel intensities to the mean of the intensities (s/m):

$$\frac{s}{m} = \frac{\text{st. dev.}(y)}{\text{mean}(y)} \quad (9)$$

where the random variable y denotes pixel intensity. Given the measurements HH , HV , and VV , we wish to construct an image from the quadratic

$$y = \mathbf{Y}^T \mathbf{A} \mathbf{Y} = g \mathbf{X}^T \mathbf{A} \mathbf{X} \quad (10)$$

where \mathbf{A} is a weighting matrix that is assumed to be Hermitian symmetric and positive definite, thus keeping y positive. To find the optimal weighting matrix \mathbf{A}^* (i.e., the one that results in an image whose pixel intensities have the minimum possible s/m), we use the following results from Ref. 8:

$$E(\mathbf{X}^T \mathbf{A} \mathbf{X}) = \text{tr}(\mathbf{\Sigma} \cdot \mathbf{A}) = \sum_{i=1}^3 \lambda_i \quad (11)$$

$$\text{VAR}(\mathbf{X}^T \mathbf{A} \mathbf{X}) = \text{tr}(\mathbf{\Sigma} \cdot \mathbf{A})^2 = \sum_{i=1}^3 \lambda_i^2 \quad (12)$$

where E is the expected value, tr is the trace, VAR is the variance, and λ_1 , λ_2 , and λ_3 are the eigenvalues of the matrix $\mathbf{\Sigma} \cdot \mathbf{A}$. Combining Eqs (7) through (12) yields

$$\begin{aligned} \left(\frac{s}{m}\right)^2 &= \left[\frac{\text{VAR}(y)}{E^2(y)}\right] = \left[\frac{E(g^2)}{E^2(g)} \cdot \frac{\text{VAR}(\mathbf{X}^T \mathbf{A} \mathbf{X})}{E^2(\mathbf{X}^T \mathbf{A} \mathbf{X})} + \frac{\text{VAR}(g)}{E^2(g)}\right] \\ &= \left[\frac{\nu + 1}{\nu} \cdot \frac{\sum_{i=1}^3 \lambda_i^2}{\left(\sum_{i=1}^3 \lambda_i\right)^2} + \frac{1}{\nu}\right] \end{aligned} \quad (13)$$

Note in Eq. (13) that ν is a constant. Therefore, minimizing s/m is equivalent to minimizing

$$\frac{\sum_{i=1}^3 \lambda_i^2}{\left(\sum_{i=1}^3 \lambda_i\right)^2} \quad (14)$$

If λ , such that $\lambda' = [\lambda_1, \lambda_2, \lambda_3]$ is a minimizing solution of (14), then so is $\alpha\lambda$, where α is a real scalar. Therefore, we can minimize (14) by minimizing its numerator

$$\left(\sum_{i=1}^3 \lambda_i^2\right) \quad (15)$$

with the following constraint on its denominator

$$\left(\sum_{i=1}^3 \lambda_i\right)^2 = 1 \quad (16)$$

Using a Lagrange multiplier, β , we minimize the unconstrained functional

$$f(\lambda) = \sum_{i=1}^3 \lambda_i^2 + \beta \left(1 - \left(\sum_{i=1}^3 \lambda_i\right)^2\right) \quad (17)$$

Taking partial derivatives with respect to λ , yields

$$\frac{\partial f(\lambda)}{\partial \lambda_i} = 2\lambda_i - 2\beta \sum_{i=1}^3 \lambda_i = 0; i = 1, 2, 3 \quad (18)$$

Thus we find that

$$\beta = \frac{\lambda_1}{\sum_{i=1}^3 \lambda_i} = \frac{\lambda_2}{\sum_{i=1}^3 \lambda_i} = \frac{\lambda_3}{\sum_{i=1}^3 \lambda_i} \quad (19)$$

which implies that

$$\lambda_1 = \lambda_2 = \lambda_3 \quad (20)$$

is a minimizing solution. The optimal weighting matrix \mathbf{A}^* is the one that causes the eigenvalues to $\mathbf{\Sigma} \cdot \mathbf{A}$ to all be equal. Therefore, a minimizing solution is

$$\mathbf{A}^* = \mathbf{\Sigma}^{-1} \quad (21)$$

The solution derived above is equivalent to applying a whitening filter to the polarimetric vector \mathbf{Y} before forming the image (see Fig. 4). In the whitening process, the vector \mathbf{Y} is passed through the filter $\mathbf{\Sigma}^{-1/2}$ to obtain

$$\mathbf{W} = \mathbf{\Sigma}^{-1/2} \mathbf{Y} = \sqrt{\gamma} \mathbf{\Sigma}^{-1/2} \mathbf{X} \quad (22)$$

The elements of \mathbf{W} are complex random variables with equal expected power. The covariance of \mathbf{W} is a scaled identity matrix; thus \mathbf{W} is said to be white. As shown in Fig. 4, the optimal solution to the polarimetric speckle-reduction problem is simply to noncoherently sum the powers in the elements of \mathbf{W} :

$$y = \mathbf{W}^T \mathbf{W}, \quad (23)$$

hence the name polarimetric whitening filter (PWF).

The process shown in Fig. 4 can also be interpreted as a change of polarimetric basis from a linear polarization basis (HH , HV , VV) to a new basis given by

$$\left[HH, \frac{HV}{\sqrt{\epsilon}}, \frac{(VV - \rho^* \sqrt{\gamma} HH)}{\sqrt{\gamma(1 - |\rho|^2)}}\right]. \quad (24)$$

In this new basis, the three polarimetric channels are uncorrelated and have equal expected power. Thus the optimal way to reduce speckle polarimetrically is to sum the powers noncoherently in these three polarimetric channels.

We have shown that the PWF algorithm processes the polarimetric measurement vector \mathbf{Y} in a way that minimizes SAR image speckle. Furthermore, the PWF is the maximum-

POLARIMETRIC WHITENING FILTER

• SIMPLE INTERPRETATION

$$Y = \begin{bmatrix} HH \\ HV \\ VV \end{bmatrix} \Rightarrow \sum_c^{-1/2} \text{ "WHITENING" FILTER} \Rightarrow W = \begin{bmatrix} HH \\ HV \\ VV - p^* \sqrt{Y} HH \\ \sqrt{Y(1-|p|^2)} \end{bmatrix} \text{ UNCORRELATED IMAGES}$$

• PWF IMAGE

$$y = |HH|^2 + \left| \frac{HV}{\sqrt{V}} \right|^2 + \left| \frac{VV - p^* \sqrt{Y} HH}{\sqrt{Y(1-|p|^2)}} \right|^2$$

Figure 4. Minimum-speckle image processing. Y is a complex vector containing the three linear-polarization measurements. Using the whitening filter gives a new polarization basis W . In this basis the three elements are uncorrelated and have equal expected power. The PWF image, y , is the noncoherent sum of the uncorrelated images.

likelihood estimate (MLE) of the spatial multiplier g . The MLE can also be shown to be an unbiased, minimum-variance estimator of g (i.e., it achieves the Cramer-Rao lower bound) (see Appendix 1).

Next we theoretically determine the amount of speckle reduction that can be achieved by using the PWF. Although the PWF solution is independent of the PDF of the spatial multiplier g in the product model, the resulting s/m ratio after speckle reduction does depend upon $f_c(g)$. Thus, the s/m for the PWF is

$$\left(\frac{s}{m} \right)_{PWF} = \sqrt{\frac{1}{3} \left(1 + \frac{4}{\nu} \right)} = \sqrt{\frac{1}{\nu} + \frac{1}{3} \left(1 + \frac{1}{\nu} \right)} \quad (25)$$

and the s/m for a single-polarimetric-channel HH image is

$$\left(\frac{s}{m} \right)_{HH} = \sqrt{1 + \frac{2}{\nu}} = \sqrt{\frac{1}{\nu} + \left(1 + \frac{1}{\nu} \right)}. \quad (26)$$

The ν parameter of the gamma multiplier appears in Eqs. (25) and (26) because the s/m includes fluctuations in the texture variable g . For an ideal speckle-free image, in fact, fluctuations in the terrain reflectivity across the image are still present, thus, its s/m is given by

$$\left(\frac{s}{m} \right)_{ideal} = \sqrt{\frac{1}{\nu}}. \quad (27)$$

The ν parameter is closely related to the log standard deviation (σ_c in dB) of the texture component of the clutter. This relation is derived in Appendix 2, and values of the ν parameter for clutter regions that have σ_c of 1 dB to 3 dB are tabulated. By using Eqs. (25) and (26) and the results given in Appendix 2, we can calculate the reduction in the standard-deviation-to-mean ratio achieved with the PWF (relative to a single-polarimetric-channel image). For clutter with a spatial log standard deviation of 1 dB, the s/m ratio of single-channel data is 1.66 times larger than the s/m ratio of PWF data. For

clutter with a spatial log standard deviation of 3 dB, the s/m ratio of single-channel data is 1.45 times larger than that of PWF data. In the next section, these theoretical predictions will be compared with measurements made on actual data.

IV. SPECKLE REDUCTION RESULTS

In the preceding section, we determined that the optimum polarimetric processing for speckle reduction is the PWF, and we derived formulas to calculate the amount of speckle reduction achievable by using the PWF. In this section we show typical imagery gathered by the Lincoln Laboratory SAR and visually compare single-polarimetric-channel imagery with PWF-processed imagery; then we use actual clutter data to calculate typical polarization covariances of trees, grass, mixed scrub, and shadows; finally, we apply PWF processing to these clutter data and compare the actual amount of speckle reduction with theoretical predictions based upon previously derived formulas [Eqs. (25) and (26)].

A. Typical SAR Imagery. Figure 5 shows another SAR image of the golf course—this image was constructed by first reducing speckle polarimetrically (using PWF processing while preserving the $1 \text{ ft} \times 1 \text{ ft}$ resolution) and then using noncoherent spatial averaging of the $1 \text{ ft} \times 1 \text{ ft}$ PWF pixel intensities into effective $1 \text{ m} \times 1 \text{ m}$ resolution pixels. The area of the image shown in Fig. 5 is approximately $500 \times 500 \text{ m}$. Clearly visible in the SAR image are the pond and several sets of trees, as well as the putting green located next to the fairway, and a larger set of trees located below the golf course. Figure 6 shows an aerial photograph of the golf course that was imaged by the Lincoln Lab SAR sensor. Note that, although the aerial photograph gives an excellent image of the golf course under conditions of good visibility, only the SAR image would be unaffected by such phenomena as rain, cloud cover, or fog.

Figure 7 displays a SAR image of a highway overpass scene ($1 \text{ ft} \times 1 \text{ ft}$ resolution). Clearly visible in the SAR image are the guardrails on each side of the overpass and the high energy returns due to the columns directly beneath the overpass. Figure 8 shows an optical photograph of the highway overpass and we can see these supporting structures. We theorize that the road beneath the overpass and the cylindrical concrete pillars create a top-hat reflector; multipath returns from these top-hat reflectors appear in the SAR image as bright returns, displaced in range (Fig. 7).

B. Comparison of HH and PWF Imagery. Figure 9 displays a SAR image (HH polarization) of the powerline tower scene ($1 \text{ m} \times 1 \text{ m}$ resolution). Clearly visible in the upper and lower portions of the image are two regions of trees separated by a narrow strip of coarse scrub. Also visible in the image, though somewhat faint, are four powerline towers positioned in the scrub region (one pair of towers in the upper left of the image and one pair in the lower right).

Figure 10 shows the corresponding PWF processed image of the powerline tower scene. Note that in the PWF processed image, the powerline towers have much greater intensity than they had in the single polarimetric channel HH image (Fig. 9). In Fig. 11, we give a graphical example of how the powerline tower and scrub clutter distributions are changed by polarimetric processing. In particular, we show histograms of



Figure 5. SAR image of the golf course scene (1 m \times 1 m resolution) corresponding to the aerial photograph shown in Figure 6. This image was formed by first applying PWF processing to the 1 ft coherent data, then spoiling (4 \times 4 noncoherent averaging) to an effective 1 m resolution.

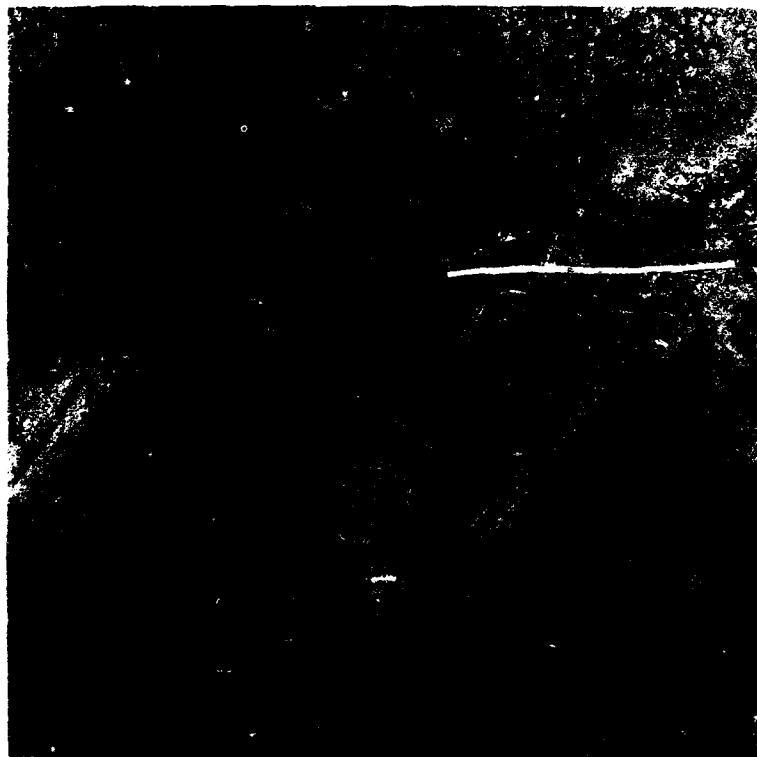


Figure 6. Aerial photograph of the golf course in Figure 5. This photograph was taken in the spring of 1989. Note that, unlike radar imagery, aerial photography of this quality can only be taken under clear weather conditions.

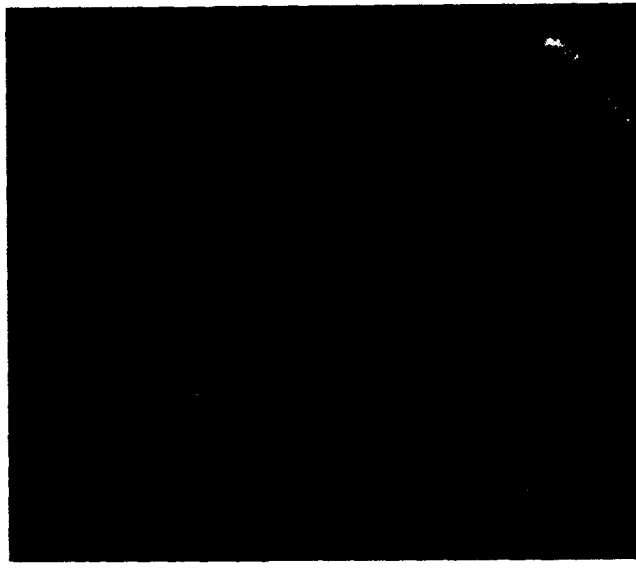


Figure 7. SAR image of a highway overpass (1 ft \times 1 ft resolution). This image taken from a stripmap containing Highway US 90 in New York, shows the detail obtained from PWF processing; note the guard rails along both sides of the overpass.

data in the powerline tower region and in the scrub region for the *HH* polarization image and for the PWF processed image. Clearly, the histograms for the PWF-processed data exhibit much less intensity variation than do the histograms for the *HH* polarized data. In addition, since the PWF greatly reduces speckle in the scrub region, the features of the project-

ed target shadow are easily discerned. Figure 12 shows a 1 ft \times 1 ft resolution image of the powerline tower and its shadow projected onto the ground. Notice the intricate shadow structure in the area below the tower in this image, and the corresponding physical structure of the actual tower as shown in Figure 13.



Figure 8. Optical photograph of one side of the highway overpass (this photograph was taken in November 1991). Note the placement of the cylindrical support structures which form top-hat reflectors with the road.

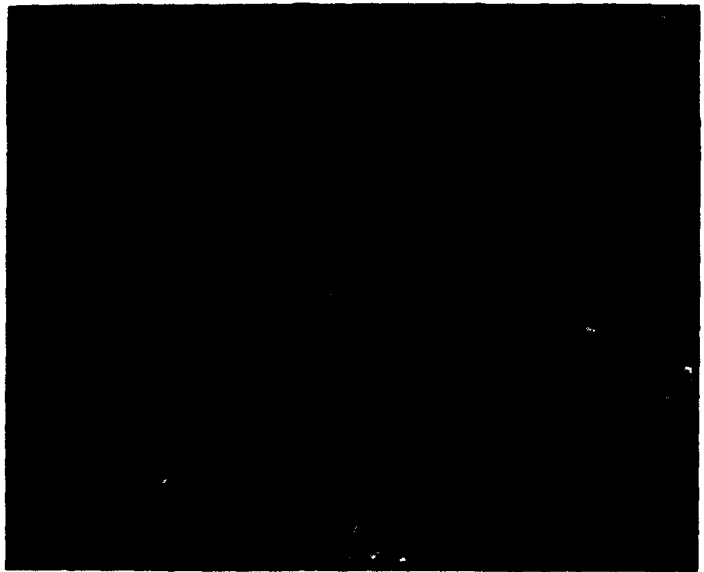


Figure 9. HH SAR image of the powerline towers in a coarse scrub region. (1 m \times 1 m resolution). Two pairs of powerline towers are visible in the scene, with one pair positioned at either end of the narrow strip of coarse scrub running diagonally through the image.

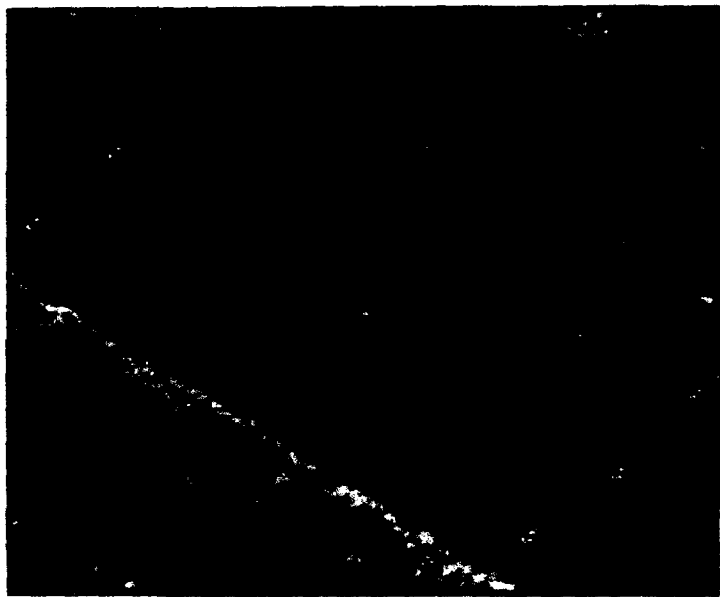


Figure 10. PWF SAR image of the powerline towers (1 m \times 1 m resolution). Note that the towers have much greater intensity than they have in the HH image shown in Figure 9.

PIXEL INTENSITY DISTRIBUTIONS

POWERLINE TOWER AREA 1 ft × 1 ft RESOLUTION

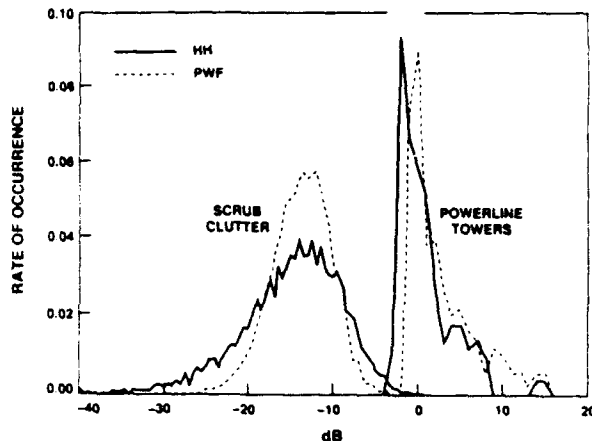


Figure 11. Histograms of powerline tower data (1 ft × 1 ft resolution) and scrub clutter data for single-channel HH image (solid curves) and for PWF processed image (dashed curves).



Figure 12. SAR image of a single powerline tower and its shadow projected onto the ground. Visible in the lower portion of the shadow is the outline of the upper support structure of the tower, including the insulators.

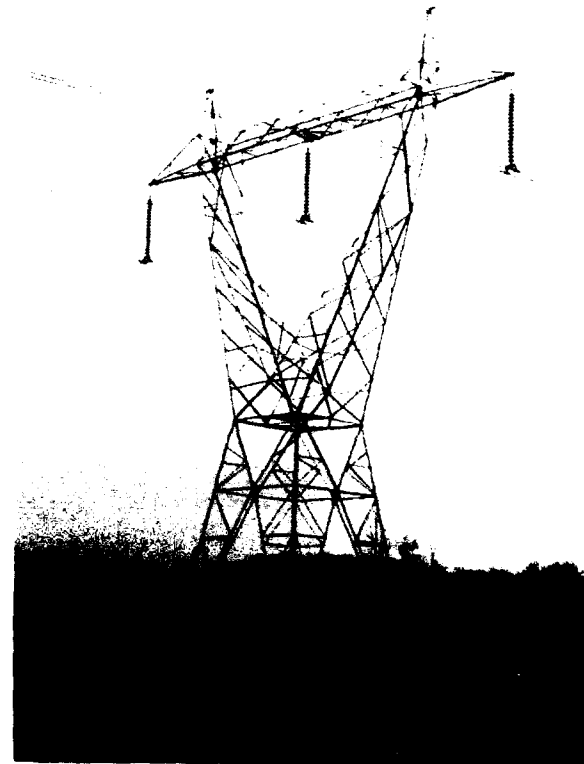


Figure 13. Photograph of the powerline tower whose SAR signature and shadow were shown in Figure 12.

C. Polarization-Covariance Calculations. The data used in this experiment were collected near Stockbridge, NY in the spring of 1989. The scrub region located in the vicinity of the powerline towers (Fig. 10) was used as one of our typical clutter backgrounds—we calculated its polarization covariance, Σ_c , to be

$$\Sigma_c = 0.098 \cdot \begin{bmatrix} 1.00 + j0.00 & 0.01 + j0.02 & 0.60 - j0.05 \\ 0.01 - j0.02 & 0.19 + j0.00 & 0.00 - j0.00 \\ 0.60 + j0.05 & -0.00 + j0.00 & 1.08 + j0.00 \end{bmatrix} \quad (28)$$

Note that the polarization covariance for scrub clutter may be approximated (quite accurately) by the general form described previously [Eqs. (4) and (5)].

Next we evaluated the polarization covariances of tree, grass, and shadow regions. For each region, we estimated the clutter polarization covariance parameters σ_{mm} , ϵ , γ , and ρ as defined in Eq. (5); these estimates are given in Table I. Although the quantity $\rho\sqrt{\gamma}$ in Table I is complex, we find for natural ground clutter that the imaginary part is negligibly small.

The polarization-covariance parameters of manmade targets are quite different from those of trees, grass, and other types of clutter. For convenience, we considered the powerline towers shown in Figs. 9 and 10 to be our hypothetical

Table I. Polarization covariance parameters of (1 ft \times 1 ft) clutter data

	σ_{HH}	ϵ	γ	ρ_{HV}
Trees	0.256	0.16	0.89	0.61
Scrub	0.098	0.19	1.08	0.60
Grass	0.086	0.19	1.03	0.53
Shadow	0.006	0.43	1.18	0.49

targets of interest. We estimated the polarization covariance of our hypothetical targets from several hundred bright peaks in the vicinity of each tower. The value obtained for Σ was:

$$\Sigma = 1.89 \cdot \begin{bmatrix} 1.00 + j0.00 & 0.20 + j0.25 & 0.39 + j0.07 \\ 0.20 + j0.25 & 1.40 + j0.00 & 0.01 + j0.16 \\ 0.39 + j0.07 & 0.01 + j0.16 & 0.99 + j0.00 \end{bmatrix} \quad (29)$$

From the above polarization covariance matrix we see that $E(HV) = 1.4 E(HH)$, which implies that the powerline towers give an unusually large HV -polarized return. This is due to the physical structure of the towers. As shown in Fig. 13, the tower frames are reinforced with steel-strut lattices oriented at many different angles. Also, from the above polarization covariance matrix we see that HV is correlated with HH and VV .

D. PWF Speckle Reduction. To validate the speckle-reduction formulas derived previously, we selected four clutter regions—shadow, grass, scrub, and trees. For each region we calculated standard-deviation-to-mean ratios for HH , HV , and VV data, and for the PWF data. The s/m ratios of clutter data given in Table II show lower—and better—numbers for the PWF-processed data.

The single-polarimetric-channel s/m ratios given in Table II can be used to compute the rms standard-deviation-to-mean ratio for each clutter region. Eq. (26) was used to estimate the approximate ν for each region, and Eq. (25) was used to predict the s/m of the PWF data. Table III compares the theoretical predictions with the actual measured values. The agreement between the theory and measurements is very good—within 5% in all cases.

Although the s/m ratios given in Table II clearly show that the PWF reduces SAR speckle, the more important question is whether the clutter log standard deviation has a corresponding decrease, because the log standard deviation directly affects target-detection performance. Shown in Table IV are the log standard deviations computed from the 1-ft resolution HH , HV , and VV data, and the 1-ft PWF data. The PWF reduces the log standard deviation by approximately 2.0 to 2.7 dB compared with single-channel 1 ft data.

Table II. s/m Ratios of (1 ft \times 1 ft) clutter data.

	HH	HV	VV	PWF
Trees	1.59	1.69	1.39	1.10
Scrub	1.43	1.27	1.38	0.94
Grass	1.12	1.06	1.16	0.67
Shadow	0.99	0.99	1.02	0.60

Table III. s/m Ratios—theory vs. measurement

	Predicted	Measured
Trees	1.13	1.10
Scrub	0.90	0.94
Grass	0.79	0.67
Shadow	0.58	0.60

Table IV. Standard deviations (dB) of (1 ft \times 1 ft) clutter data

	HH	HV	VV	PWF
Trees	6.67	6.14	6.35	4.13
Scrub	6.28	6.00	6.36	3.00
Grass	5.67	5.59	5.67	2.97
Shadow	5.20	5.24	5.46	2.81

E. PWF Versus Adaptive PWF Comparison. In Ref. 3 an adaptive PWF algorithm was proposed and analyzed. This algorithm adaptively estimates polarization covariances of various regions of clutter over the image and uses these same estimated covariances to minimize the speckle within each clutter region. Since the polarization covariances of grass, trees, and shadow regions were found to be very similar (Table I), we investigated the improvement in speckle reduction achievable using adaptive PWF processing.

We compared the log standard deviation of the clutter regions after they were whitened with the covariance of grass, versus the result when they were whitened with the proper covariance (e.g., trees whitened with tree covariances). As the data in Table V indicate, the use of the proper covariances made virtually no change in the log standard deviations. Thus, because the covariances of the different regions are so similar, the extra computation required for adaptive PWF processing is not warranted.

F. Polarimetric Averaging Versus Spatial Averaging. As mentioned earlier, speckle can be reduced by noncoherent spatial averaging, or spoiling, of the high-resolution SAR intensity data; however, noncoherent spatial averaging degrades image resolution. The log standard deviations of 1 ft and 1 m PWF data are clearly superior to the log standard deviation of 1 ft and 1 m single polarimetric-channel data, as is shown by the results presented in Table VI.

For grass regions, PWF data at 1 ft resolution were measured to have a log standard deviation of 2.0 dB. At the same resolution, the HH data were measured to have a log standard deviation of 5.7 dB and the HV data had a log standard deviation of 5.6 dB. Thus polarimetric averaging improved the results over single-channel data by 2.7 dB. Noncoherently spoiling the single-channel data to 1 m resolution (i.e., 4 \times 4 averaging) reduced σ_e by approximately 3.7 dB, 1 dB better than polarimetric averaging—but image resolution was sac-

Table V. Standard deviations (dB) of PWF vs. adaptive PWF data.

	PWF	APWF
Trees	4.13	4.10
Scrub	3.90	3.89
Grass	2.97	2.97
Shadow	2.18	2.17

Table VI. Standard deviations (dB) of 1-ft- and 1-m-resolution data.

	1-ft HH	1-ft PWF	1-m HH	1-m PWF
Trees	6.7	4.1	3.5	2.8
Grass	5.7	3.0	2.0	1.3
Shadow	5.2	2.8	1.7	1.0

rified for the improvement. Spoiling the PWF data to 1-m resolution yielded the clutter log standard deviation of 1.3 dB, an 0.7 dB improvement over the 1-m *HH* data, and an 0.5-dB improvement over the 1-m *HV* data. Similar results were obtained for tree clutter and for shadows.

SUMMARY

We investigated the polarimetric speckle reduction that is achieved by using the polarimetric whitening filter (PWF); this processing method reduces SAR image speckle without degrading the spatial resolution of the image. Results obtained with actual SAR data show that the PWF reduced speckle—and it also significantly reduced clutter log standard deviation. At 1 ft \times 1 ft resolution, the log standard deviation of clutter was reduced by approximately 2.5 dB relative to a single polarimetric channel. Such an improvement in log standard deviation has been shown to improve target detection performance [8, 9]. PWF processing has also been shown to significantly improve the performance of clutter segmentation [10] and texture discrimination algorithms [11].

Other researchers have applied PWF, adaptive PWF, and other polarimetric processing methods to multifrequency polarimetric SAR data. A brief discussion of some of this important research is given in the following paragraphs.

Toma et al. [13] developed a method for reducing speckle in SAR intensity imagery using multifrequency, fully polarimetric SAR data; their method, which is a straightforward extension of the PWF, was applied to 4 m \times 4 m resolution data gathered by the Jet Propulsion Laboratory (JPL) airborne SAR [14]. The three complex polarimetric measurements (*HH*, *HV*, and *VV*) simultaneously gathered at *P*-, *L*-, and *C*-bands were combined into a 9-dimensional measurement vector:

$$\mathbf{Y}' = (HH_p, HV_p, VV_p, HH_l, HV_l, VV_l, HH_c, HV_c, VV_c) \quad (30)$$

Then a 9 \times 9 whitening filter was applied to the complex data to obtain nine uncorrelated intensity images. Noncoherent averaging of these nine images produced a SAR intensity image having an amount of speckle reduction equivalent to that obtained by averaging nine independent samples.

Lee et al. [15] also developed a method for reducing speckle in SAR intensity imagery using multifrequency, fully polarimetric SAR data; they also applied their method to JPL SAR data. The method does not use the complex *HH*, *HV*, and *VV* data, but instead uses the polarimetric intensity data ($|HH|^2$, $|HV|^2$, and $|VV|^2$) to achieve speckle reduction. For each single-frequency-band (*P*-, *L*-, and *C*-), a weighted linear combination of the form

$$y = |HH|^2 + k_2|HV|^2 + k_3|VV|^2 \quad (31)$$

was used to construct a reduced-speckle SAR intensity image,

y. The coefficients k_2 and k_3 were selected to minimize a mean-square-error cost function (see Appendix A of Ref. 15 for details).

Since Eq. (31) is a weighted average of three correlated images, one would not expect to achieve as much speckle reduction as that obtained by averaging three independent samples. The *P*-, *L*-, and *C*-band intensity images produced using Eq. (31) were combined using a weighted average similar to Eq. (31). This final SAR intensity image was observed to have an amount of speckle reduction equivalent to that obtained by averaging six independent samples. Recall that the approach of Toma et al. [13] provided an amount of speckle reduction equivalent to that obtained by averaging nine independent samples.

The reason for the difference in speckle reduction is that Lee, et al. used *HH* and *VV* data, which are correlated. Toma et al. used a whitening filter to produce nine uncorrelated (independent) samples.

In our studies, adaptive PWF processing provided a marginal improvement in speckle reduction (Table V shows these results). This is in agreement with the findings of Lee et al. and Toma et al. However, adaptive processing has been found to blur imagery, especially near sharp contrast edges [8] (nonadaptive PWF processing produces very clear imagery, as is shown in this article). Also, adaptive PWF processing has been shown to produce degraded target detection performance compared with nonadaptive PWF processing [8].

APPENDIX 1: THE PWF AS AN ESTIMATOR

In this appendix, we show that for a given polarimetric measurement vector \mathbf{Y} , the PWF is the maximum-likelihood estimate (MLE) of the clutter texture parameter g . We also show that the PWF is an unbiased, minimum-variance estimator (i.e., it achieves the Cramer-Rao lower bound) of the texture parameter g .

A. Maximum-Likelihood Estimate. In MLE, the parameter g is treated as if it were deterministic (nonrandom) but unknown. We seek the value of parameter g that makes the observed vector \mathbf{Y} most likely. If we denote the MLE of g for a given \mathbf{Y} by g_{MLE} , then g_{MLE} is implicitly defined by

$$\frac{\partial}{\partial g} p(\mathbf{Y} | g) \Big|_{g=g_{MLE}} = 0 \quad (32)$$

where $p(\mathbf{Y} | g)$ is the conditional probability density function (PDF) of the vector \mathbf{Y} given g . This conditional PDF is easy to evaluate since, given g , the vector \mathbf{Y} is complex Gaussian with mean 0 and covariance $g\Sigma$. Thus

$$p(\mathbf{Y} | g) = \frac{1}{\pi^p |\Sigma|^p} \exp(-\mathbf{Y}^* \Sigma^{-1} \mathbf{Y} / g) \quad (33)$$

where p = the number of polarizations (*HH*, *HV*, and *VV*; thus p = 3 in our case). To obtain the MLE, we need to find the value of g for which $p(\mathbf{Y} | g)$ is maximum. Equivalently, we can find the value of g for which $\log p(\mathbf{Y} | g)$ is maximum.

$$\log[p(\mathbf{Y} | g)] = -\log(\pi^p |\Sigma|) - p \log g - \mathbf{Y}^* \Sigma^{-1} \mathbf{Y} / g. \quad (34)$$

Differentiating with respect to g yields

$$\frac{\partial}{\partial g} \log[p(\mathbf{Y} | g)] = -\frac{p}{g} + \frac{\mathbf{Y}' \boldsymbol{\Sigma}^{-1} \mathbf{Y}}{g^2} = 0$$

$$g_{\text{MLE}} = \mathbf{Y}' \boldsymbol{\Sigma}^{-1} \mathbf{Y} p, \quad (35)$$

which is precisely the PWF solution.

Cramer-Rao Bound. Next, we investigate the estimate g_{MLE} and determine (1) that the estimate is unbiased, and (2) that the estimate achieves the Cramer-Rao lower bound on variance of the error (thus g_{MLE} is an efficient estimate of the texture parameter g).

First we demonstrate that g_{MLE} is unbiased. From Eq. (35) we have

$$g_{\text{MLE}} = \frac{1}{p} \mathbf{Y}' \boldsymbol{\Sigma}^{-1} \mathbf{Y} = \frac{1}{p} g \mathbf{X}' \boldsymbol{\Sigma}^{-1} \mathbf{X}. \quad (36)$$

Taking the expectation with respect to \mathbf{X} gives

$$E(g_{\text{MLE}}) = \frac{1}{p} g E(\mathbf{X}' \boldsymbol{\Sigma}^{-1} \mathbf{X}). \quad (37)$$

But Eq. (11) gives

$$E(\mathbf{X}' \boldsymbol{\Sigma}^{-1} \mathbf{X}) = \text{tr}[\boldsymbol{\Sigma}^{-1} E(\mathbf{X} \mathbf{X}')] \quad (38)$$

$$= \text{tr}(\boldsymbol{\Sigma}^{-1} \boldsymbol{\Sigma}) = p.$$

Thus we have verified that the MLE estimate, g_{MLE} , is unbiased. That is,

$$E(g_{\text{MLE}}) = g. \quad (39)$$

Next we verify that g_{MLE} satisfies the Cramer-Rao lower bound, which states that the variance of any unbiased estimate, \hat{g} must satisfy the inequality

$$\text{VAR}(\hat{g}) \geq \frac{-1}{E\left\{ \frac{\partial^2}{\partial g^2} \log[p(\mathbf{Y} | g)] \right\}}. \quad (40)$$

Omitting the details of the derivation, one may easily show that

$$\frac{\partial^2}{\partial g^2} \log[p(\mathbf{Y} | g)] = \frac{p}{g^3} - \frac{2\mathbf{Y}' \boldsymbol{\Sigma}^{-1} \mathbf{Y}}{g^3}. \quad (41)$$

Evaluating the expectation of the above, again using Eq. (11), yields the result

$$E\left\{ \frac{\partial^2}{\partial g^2} \log[p(\mathbf{Y} | g)] \right\} = \frac{-p}{g^2}. \quad (42)$$

Thus the variance of any unbiased estimator of the texture parameter g must satisfy the Cramer-Rao bound

$$\text{VAR}(\hat{g}) \geq \frac{g^2}{p}. \quad (43)$$

Finally, we can verify that the unbiased estimate g_{MLE} achieves the lower bound.

$$\begin{aligned} \text{VAR}(g_{\text{MLE}}) &= \text{VAR}\left(\frac{1}{p} g \mathbf{X}' \boldsymbol{\Sigma}^{-1} \mathbf{X}\right) \\ &= \frac{g^2}{p^2} \text{VAR}(\mathbf{X}' \boldsymbol{\Sigma}^{-1} \mathbf{X}) \end{aligned} \quad (44)$$

Evaluating the above, using Eq. (12) yields the result

$$\text{VAR}(g_{\text{MLE}}) = \frac{g^2}{p}. \quad (45)$$

APPENDIX 2: RELATING σ_c AND ν

The log standard deviation of the texture variable g (denoted σ_c) is defined to be

$$\sigma_c = \sqrt{\text{VAR}(10 \log_{10} g)}. \quad (\text{dB}) \quad (46)$$

The relation between σ_c and the shape parameter ν of the gamma PDF can be described as

$$E(\log g) = \frac{1}{\Gamma(\nu) \bar{g}^\nu} \int_0^\infty (\log g) g^{\nu-1} \exp\left(-\frac{g}{\bar{g}}\right) dg. \quad (47)$$

From Ref. 12 [Eq. (4.352.1)] we have

$$E(\log g) = \Psi(\nu) + \log \bar{g} \quad (48)$$

$$E[(\log g)^\nu] = \frac{1}{\Gamma(\nu) \bar{g}^\nu} \int_0^\infty (\log g)^\nu g^{\nu-1} \exp\left(-\frac{g}{\bar{g}}\right) dg. \quad (49)$$

Ref. 12 [Eq. (4.358.2)] also gives

$$E[(\log g)^\nu] = [\Psi(\nu) + \log \bar{g}]^\nu + \zeta(2, \nu). \quad (50)$$

Thus

$$\text{VAR}(\log g) = \zeta(2, \nu) \quad (51)$$

and

$$\text{VAR}(10 \log_{10} g) = \text{VAR}\left(\frac{10 \log g}{\log 10}\right) = (4.34)^2 \zeta(2, \nu). \quad (52)$$

where from Ref. 12 [Eq. (9.521.1)]

$$\zeta(2, \nu) = \sum_{n=0}^{\infty} \frac{1}{(\nu + n)^2} \quad (53)$$

Table VII lists the value of the gamma parameter as a function of the clutter standard deviation for some typical clutter standard deviations.

Table VII. Gamma parameter (ν) versus σ_c (dB)

σ_c	ν
1.0	19.3
1.5	8.9
2.0	5.2
2.5	3.5
3.0	2.6

ACKNOWLEDGMENTS

The Lincoln Laboratory SAR and special-purpose ground processing equipment were built by the Loral Corporation of Phoenix, Arizona. The intensity-to-color transformation used to display the imagery herein was also developed by Loral—this intensity-to-color transformation is available upon request. The authors also wish to acknowledge contributions by their colleagues Michael C. Burl, Gregory J. Owirka, and Shawn M. Verbout.

REFERENCES

1. J. C. Henry, T. J. Murphy, and K. M. Carusone "The Lincoln Laboratory millimeter-wave SAR imaging system," *SPIE Conf. SAR*, Los Angeles, CA, January 1992.
2. R. M. Barnes and D. J. Blejer, "Polarimetric SAR antenna characterization," Project Report STD-15, MIT Lincoln Laboratory (28 July 1989). DTIC #ESD-TR-89-166.
3. L. M. Novak and M. C. Burl, "Optimal speckle reduction in polarimetric SAR imagery," *IEEE Trans Aerospace Electron Syst.*, (1990).
4. L. M. Novak and M. C. Burl, "Optimal speckle reduction in POL-SAR imagery and its effect on target detection," *Proc. SPIE Conf. Polarimetry* (1989).
5. L. M. Novak, M. B. Sechtin, and M. J. Cardullo, "Studies of target detection algorithms that use polarimetric radar data," *IEEE Trans. Aerospace Electron. Syst.* (1989).
6. E. Jakeman and P. N. Pusey, "A Model for non-Rayleigh sea echo," *IEEE Trans. Antennas and Propagation* (1976).
7. J. K. Jao, "Amplitude distribution of composite terrain radar clutter and the K-distribution," *IEEE Trans. Antennas and Propagation* (1984).
8. L. M. Novak, M.C. Burl, and W.W. Irving "Optimal polarimetric processing for enhanced target detection," *IEEE Trans. Aerospace and Electron Syst.* (January 1993).
9. R. D. Chaney, M. C. Burl, and L. M. Novak, "On the performance of polarimetric target detection algorithms," *Proc. 1990 IEEE Int'l. Radar Conf.*, Arlington, VA (May 1990).
10. M. C. Burl and L. M. Novak, "Polarimetric segmentation of SAR imagery," *SPIE Conf. Automatic Object Recognition*, Orlando, FL (1991).
11. M. C. Burl, G. J. Owirka, and L. M. Novak, "Texture discrimination in synthetic aperture radar imagery," *Proc. 23rd Asilomar Conf. Signals, Systems, and Computers*, Pacific Grove, CA (November 1989).
12. I. S. Gradshteyn and I. M. Ryzhik, *Table of Integrals, Series, and Products* (Academic Press, New York, 1980).
13. M. R. Toma, F. Vinelli, A. Farina, and A. Forte, "Processing polarimetric and multifrequency SAR data recorded by Maestro-1 campaign," *Proc. IGARSS Conf.* (1991).
14. D. N. Held et al., "The NASA JPL, multifrequency, multipolarization, airborne SAR system," *Proc. IGARSS Conf.* (1988).
15. J. S. Lee, M. R. Grunes, and S. A. Mango, "Speckle reduction in multipolarization, multifrequency SAR imagery," *IEEE Trans. Geosci. Remote Sensing* (1991).

Accession For	
NTIS	CRA&I
DTIC	TAB
Unpublished	
Justification	
By _____	
Distribution: /	
Availability Codes	
Dist	Available and/or Special
A-1	20

DTIC QUALITY INSPECTED 8